Global Sea Surface Height Measurement From CYGNSS Based on Machine Learning

Yun Zhang, Qi Lu, Qin Jin, Wanting Meng, Shuhu Yang , Shen Huang, Yanling Han, Zhonghua Hong , Zhansheng Chen, and Weiliang Liu

Abstract—Cyclone Global Navigation Satellite System (CYGNSS) launched in recent years, provides a large amount of spaceborne GNSS Reflectometry data with all-weather, global coverage, high space-time resolution, and multiple signal sources, which provides new opportunities for the machine learning (ML) study of sea surface height (SSH) inversion. This article proposes for the first time two different CYGNSS SSH inversion models based on two widely used ML methods, back propagation (BP) neural network and convolutional neural network (CNN). The SSH calculated by using Danmarks Tekniske Universitet (DTU) 18 ocean wide mean SSH (MSSH) model (DTU18) with DTU global ocean tide model is used for verification. According to the strategy of independent analysis of data from different signal sources, the mean absolute error (MAE) of the BP and CNN models' inversion specular points' results during 7 days is 1.04 m and 0.63 m, respectively. The CLS 2015 product and Jason-3 data were also used for further validation. In addition, the generalization ability of the model, for 6 days and 13 days training sets, was also evaluated. For 6 days training set, the prediction results' MAE of the BP model is 11.59 m and 5.90 m for PRN2 and PRN4, and the MAE of the CNN model is 1.37 m and 0.97 m for PRN2 and PRN4, respectively. The results show that BP and CNN inversions are in high agreement with each product, and the CNN model has relatively higher accuracy and better generalization ability.

Index Terms—Back propagation (BP), convolution neural network (CNN), cyclone global navigation satellite system (CYGNSS), global navigation satellite system reflectometry (GNSS-R), sea surface height (SSH).

I. INTRODUCTION

MOST of the earth's surface is covered by the ocean, the height of the sea surface and its changes are not only important for studies such as oceanography but also greatly related to the survival and development of human beings. Compared with ship measurements and satellite altimeter retrieval, spaceborne Global Navigation Satellite System Reflectometry (GNSS-R) technology has the advantages of multiple signal sources, space-time diversity, and low cost. Spaceborne GNSS-R technology is an emerging remote sensing technology that uses a satellite platform to receive GNSS satellite signals reflected from the earth surface to analyze and invert the physical information of the reflected surface. Martin-Neira [1] proposed using GPS reflection signals for sea surface height (SSH) retrieval, which was an earlier attempt of GNSS-R for ocean altimetry. This was followed by new applications in tidal [2], [3], soil moisture [4], [5], sea ice detection [6], [7], [8], and wind speed retrieval [9], [10]. Previous GNSS-R experiments have mainly focused on receiver experiments on land and the coast. In recent years, with the launch of satellites such as Techdemosat-1 (TDS-1) of Surrey Satellite Technology Limited, Cyclone Global Navigation Satellite System (CYGNSS) of National Aeronautics and Space Administration (NASA), and other satellites, the research opportunities for spaceborne GNSS-R altimetry have become more and more abundant [11], [12].

At present, the research on spaceborne GNSS-R SSH inversion is mainly based on the principle of spaceborne GNSS-R geometric relationship to build a physical model. This method uses the delay-Doppler map (DDM) to estimate the position of the retracking point and, thus, calculate the SSH. In 2016, Clarizia et al. [13] performed the first spaceborne SSH inversion using TDS-1 satellite data. Using Danmarks Tekniske Universitet (DTU) 10 ocean wide mean SSH (MSSH) model (DTU10) as a validation comparison model, the root-mean-square error (RMSE) of 8.1 m and 7.4 m was obtained using six months of TDS-1 satellite data to invert the SSH of the South Atlantic and the North Pacific, respectively. In 2020, Qiu and Jin [14] used CYGNSS data to inverse perform global sea level height by observing the relationship between waveform features in DDM and delay waveform data. The mean absolute error (MAE) compared with the cnes_cls2015 and DTU10 models was 1.33 m and 2.63 m, respectively, and the RMSE was 2.26 m and 3.56 m, with correlation coefficients of 0.97 and 0.95. In the same year, Zhang et al. [15] optimized the error correction model of spaceborne GPS-R using TDS-1 data with the DDM SSH inversion technique. The MAE of the optimized inversion model compared with the DTU15 model was 6.05 m, with a relative

improvement in accuracy of about 29%. The DDM-based SSH inversion technique complements the analysis of increasingly rich error models. Its inversion results mainly use the MSSH model as validation, and the accuracy can reach the meter level. However, many disturbances and errors in the spaceborne observations are difficult to entirely correct, and the subject of improving the accuracy of SSH inversion by traditional methods is becoming more and more complicated and tricky.

In recent years, machine learning (ML) algorithms have been gradually integrated into the GNSS-R field with their powerful nonlinear fitting ability and ease of construction. For GNSS-R wind speed inversion, Reynolds et al. [16] presented an artificial neural network (ANN) inversion algorithm for wind speed inversion based on CYGNSS satellite data. Zhang et al. [17] combined principal component analysis (PCA), support vector regression (SVR), PCA combined SVR (PCA-SVR) method, and the convolutional neural network (CNN) method, respectively, thus constructing a sea surface high wind speed inversion model. Zhang et al. [18] analyzed CYGNSS data and used the support vector machine (SVM) method for sea surface wind direction inversion. For soil moisture inversion, Senyurek et al. [19] used three widely used ML methods, ANN, random forest (RF), and SVM, for comparative analysis of soil moisture inversion. All these suggest that ML has been successfully applied to some GNSS-R studies.

In the SSH inversion study, Wang et al. [20] used airborne waveform data from the Baltic Sea to construct a new ML fusion model for SSH retrieval in 2021. Pearson correlation coefficient and PCA in combination with multiple ML models were used. Compared with the DTU15 model, the RMSE was about 0.23 m and the correlation coefficient was about 0.75. In the same year, Zhang et al. [21] analyzed TDS-1 data distributed over a vast sea area. They proposed two spaceborne SSH inversion models, PCA-SVR and CNN, and the inversion results of the models had an average MAE below 1 m compared to DTU15. These studies highlight the potential of ML algorithms in the field of GNSS-R SSH inversion research.

Since there are no SSH inversion ML model studies using CYGNSS data, this article proposes for the first time ML models for SSH inversion using CYGNSS data, which focuses on the CYGNSS data input for the ML models, structure of the ML models, the comparison of the ML models' performance, and the generalization ability of the ML models. Two different types of networks are considered for modeling SSH inversion for comparative analysis: the classical BP neural network, and the CNN. CNN includes convolutional computation and has a deep structure, which is one of the representative algorithms of deep learning. In contrast to airborne or ground-borne SSH inversion analysis, which lacks space-time diversity, this article utilizes the high-resolution spaceborne GNSS-R data provided by CYGNSS, to analyze a wide range of sea areas. Compared with TDS-1 data [21], CYGNSS has 8 GNSS-R receiving satellites and a larger number of valid samples, so CYGNSS is expected to have better accuracy, especially better generalization performance, which will be discussed as follows.
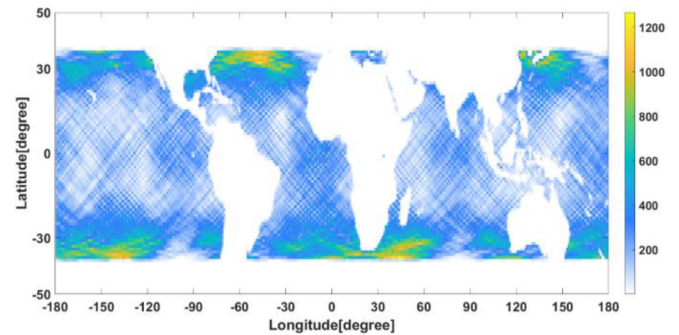

Fig. 1.   Density distribution of CYGNSS specular reflection points from August 1–7, 2020.

II. DATASETS

A. CYGNSS Data

CYGNSS was launched on December 15, 2016, and was jointly developed by NASA, the University of Michigan, and the Southwest Research Institute. CYGNSS consists of eight identical low-orbiting microsatellites, each of which has four channels that can work simultaneously, thus offering the advantage of higher spatial and temporal resolution. The satellites of CYGNSS have an orbital inclination of 35° and an altitude of 510 km. They are equipped with only one payload, the Space GPS Receiver Remote Sensing Instrument, dedicated to the GNSS reflectometry mission. Zenith GNSS antennas are mainly used to receive direct signals from GNSS satellites, and nadir antennas are high-gain reflector antennas used to receive signals from rough ocean surfaces. In this article, L1-level data from CYGNSS for the consecutive week of August 1–7, 2020, were randomly selected for analysis. Besides, DDM is the key to the traditional SSH inversion technique, and it represents the surface power received at each observed specular point for a specific time delay and Doppler frequency range [24]. The inversion of the CYGNSS forward scattering model allows for obtaining the bistatic radar cross section (BRCS) and the effective scattering area. In the L1 data, the BRCS is an 11×17 DDM array and provides some features associated with the waveform. CYGNSS L1 data are available on NASA's Physical Oceanography Distributed Activity Archive Center website, with data stored as one NC file per satellite per day. Each satellite has four channels working in parallel and can collect about 700 000 data a day. Thus, CYGNSS can accumulate about 39.2 million data a week. In addition, to ensure the reliability and accuracy of data analysis, this article filters the data using the following rules: 1) CYGNSS data quality control flag bits; 2) incidence angle less than 30°; 3) signal-to-noise ratio (SNR) greater than 5 dB. The quality flag bits filtration standards include data values of null, abnormal parameters in data observation, inability to calculate satellite state, DDM calibration error, and BRCS peak point location is significantly OFF-center and within 25 km of land.

The filtered data is more than 6.7 million items from August 1–7, 2020. Fig. 1 shows the density distribution of the specular reflection points of the dataset. The color in the figure represents
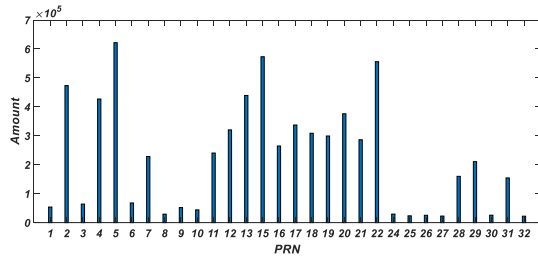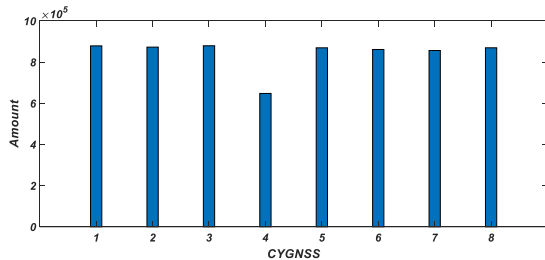
Fig. 2. Amount of data number per GPS satellite.

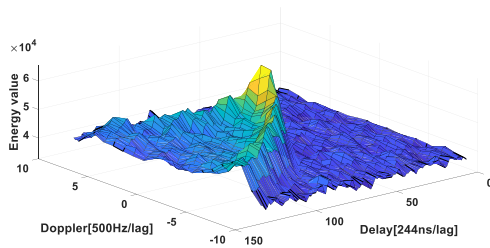
Fig. 3. Amount of data number per CYGNSS satellite.

Fig. 4. Example of a DDM.

TABLE I
SELECTED PARAMETERS AND DESCRIPTION

Parameter	Description
Tx, Ty, Tz	GPS satellites velocity in X, Y, Z
Rx, Ry, Rz	CYGNSS satellites velocity in X, Y, Z
SNR	DDM signal to noise ratio
sp_inc_angle	Specular point incidence angle
sp_rx_gain	Receiver antenna gain in the direction of the specular point
brcs_ddm_sp_bin_delay_row	BRCS DDM specular reflection point delay rows
brcs_ddm_peak_bin_delay_row	BRCS DDM peak delay rows
brcs_ddm_sp_bin_dopp_col	BRCS DDM specular reflection point Doppler columns
brcs_ddm_peak_bin_dopp_col	BRCS DDM peak Doppler columns

the revisit times in a one-degree grid. Fig. 2 counts the data distribution of the subdataset divided by different GPS satellites. In total, 32 GPS satellites are involved, but the distribution is uneven, with the most significant amount of data being 620 000 and the smallest being just over 20 000. Fig. 3 shows the data distribution of the subdata according to the different CYGNSS satellites. The data are evenly distributed among the eight CYGNSS satellites, except for satellite No. 4, which is more than 600 000, and the remaining seven are above 800 000.

B. Feature Selection

CYGNSS L1 data directly provides the locations of the BRCS DDM specular reflection point delay rows and peak delay rows, which can be used as references for calculating path delay, therefore, they can be directly used as input parameters for the ML models.

Fig. 4 shows a typical CYGNSS L1 DDM. The energy is affected by the delay effect and the Doppler effect, which is caused by the relative high-speed movement between the receiver and the transmitter, the dynamically changing direction, and the considerable satellite altitude and spacing. The integral Doppler reflects the magnitude and direction of the change in

geometric distance [21]. CYGNSS L1 data directly provides the location of the BRCS DDM specular reflection point Doppler column and the peak Doppler column, as well as the vector velocities of the transmitter and receiver satellites. Therefore, these primitive features, which are essential in the spaceborne GNSS-R observations, are also considered input parameters for the model.

In addition, the space-time span of spaceborne GNSS-R observation is relatively large, and the GNSS signal itself is more susceptible to interference. Factors such as unknown sea state and sea surface roughness can affect the reflected signal's DDM power waveform. The DDM SNR and receiver antenna gain are also considered important essential parameters in this article. All the parameters considered in the summary are shown in Table I.

C. DTU Ocean Wide MSSH Model

DTU18 is a global MSSH model developed by DTU and calculated from 17 years of data from several satellites with altimetry missions such as Jason-1, ERS-1, and ICESat. This article uses a combination of the static DTU18 MSSH and the DTU global ocean tide model to build a DTU SSH model to calculate the approximate SSH. Specifically, for the gridded product DTU18, a bilinear interpolation method was used to interpolate and match the MSSH (H_{MSSH}) based on longitude and latitude. Similarly, the DTU global ocean tide model is a gridded product, but the product itself provides an interpolation algorithm. The corresponding ocean tide height (H_{tide}) is obtained by directly inputting the latitude, longitude, and time information of the specular reflection point. Therefore, the sea surface height ($\mathrm{SSH}_{\mathrm{DTU}}$) calculated by the model can be

expressed as

$$SSH_{DTU} = H_{MSSH} + H_{Tide}. \tag{1}$$

D. MSS CLS 2015

MSS CLS 2015 is a mean sea surface model calculated using 20 years of altimetry data from 1993 to 2012, which is mainly derived from the geodetic missions of Jason-1 and CryoSat-2, with SSH estimation errors of the order of centimeters. CLS 2015 data is available in a web-based common data form format on the aviso website. CLS 2015 is a gridded MSSH model, while the inversion results are specular reflection point data. Therefore, it is necessary to first interpolate and match the longitude and latitude positions of the specular reflection points, then obtain the MSSH corresponding to the data from the CLS 2015 model.

E. Jason-3 Data

The Jason-3 satellite was launched on January 17, 2016. It was developed in collaboration with four agencies: NASA, National Oceanic and Atmospheric Administration, European Organization for the Exploitation of Meteorological Satellites, and Centre National d'Etudes Spatiales. The Jason-3 satellite orbit is a nonsun-synchronous circular orbit with an orbital altitude of 1336 km, an orbital inclination of 66.038°, and an orbital return period of 9.9 days. Jason-3 carries the Poseidon-3B altimeter, a dual-frequency, subsatellite-pointing radar altimeter that is the critical payload for the Jason-3 satellite mission. The mission goal of Jason-3 is to follow in the footsteps of TOPEX/POSEIDON, Jason-1, and Jason-2, and continue to provide continuous ocean topographic data with uniform accuracy and coverage for the study of ocean circulation and SSH. Besides, support the prediction of extreme weather conditions, oceanography, and climate variability. Although Jason-3 is used for SSH missions requiring accuracy of 3.4 cm or better, it has a lower time resolution (Jason-3 revisit period is 10 days, and CYGNSS is about 3–7 h) and costs more to measure. The geophysical data provided by Jason-3 is available on the aviso website.

Jason-3 cannot provide MSSH data directly. The distance from the satellite to the earth's surface can be calculated by the altimeter and its associated error correction data from Jason-3 data. Jason-3 also provides the distance of the satellite altimeter above the reference ellipsoid directly, and the SSH (H_{j3ssh}) can be calculated as the difference between the two values. The corresponding tidal height (H_{j3tide}) is then calculated again using the DTU global ocean tide model based on the latitude, longitude, and time of the Jason-3 data points. Finally, the MSSH (H_{j3mssh}) based on Jason-3 data can be calculated by

$$H_{j3mssh} = H_{j3ssh} - H_{j3tide} = (\text{Altitude} - \text{Range}) - H_{j3tide} \tag{2}$$

where Altitude means the distance of the satellite altimeter above the reference ellipsoid, Range means the distance from the satellite to the earth's surface.
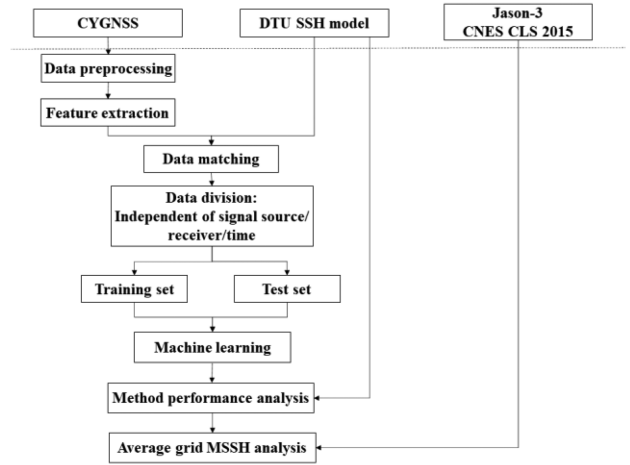

Fig. 5.   Sea surface height inversion process based on ML.

III. METHODOLOGY

Fig. 5 illustrates the SSH inversion process using CYGNSS data. Suitable relevant feature data are extracted from CYGNSS to build feature datasets, and the DTU SSH model is used to do data matching as the label of feature datasets. To validate the inversion performance of the proposed model on CYGNSS data from multiple perspectives, two approaches of data analysis were compared: 1) subdataset analysis according to the different GPS satellite PRN, 2) subdataset analysis according to the different CYGNSS satellite number. The advantage of both schemes is that the physical laws of the signal are fully considered, distinguishing between the source of signal emission and the source of data acquisition. To evaluate the generalization ability of the model, time-independent data were also tested. The whole week's data are split into a training set and a test set in date order, and the data for the first six days are used to train the model to predict the SSH for the seventh day.

In terms of methodology, two types of neural networks, BP and CNN, are used to build SSH inversion models separately for comparative analysis. In the application of neural networks, overfitting is a common potential problem. This problem occurs when a neural network has been trained to predict the output of a training dataset accurately but performs poorly on a new test dataset [16]. The dataset is randomly divided into a 20% training set and an 80% test set. The training set is further randomly divided into two subsets, each consisting of 50% of the training set. One subset is used for the error back-propagation process to train the neural network, and the other subset is used for independent validation of the network in each training iteration to observe whether the trend of error decline as the number of training iterations increases is like that of the training set, thus detecting overfitting or other problems [16]. It also facilitates a quick and efficient way to determine the optimal network structure by counting the preliminary effects of model inversions with multiple sets of different hyperparameters.

In the evaluation, not only the MAE, RMSE, but also coefficient of determination (R^2) between the model-inverted SSH and the DTU SSH model were used. R^2 reflects the degree of model
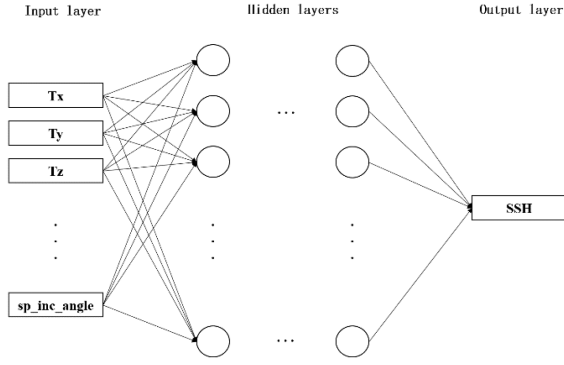
Fig. 6. Network structure model of BP.

Fig. 7. Network structure model of CNN.

fit, the closer to 1 means the better the model fit, the closer to 0 means the worse the model fit. In addition, the model-inverted SSH with tidal effects removed was evaluated for the MSSH at one-degree spatial resolution using the data products of CLS 2015 and Jason-3, respectively.

A. BP Model

BP is a multilayer feedforward neural network trained based on backpropagation learning rules. As shown in Fig. 6, the network structure of BP generally consists of three parts, including an input layer that feeds feature data, an output layer that serves as a prediction target, and a hidden layer that contains several computational units. The input layer corresponds to the 13 feature parameters selected from CYGNSS data, and the output layer is the SSH. The hidden layers can be composed of multiple layers, each layer contains several neurons, and the neurons between layers are connected according to specific weights. The first stage of the BP learning process is the forward propagation of data from the input layer to the output layer. Each neuron transforms the output in the previous layer by the activation function and then uses it as input to the neuron in the next layer. In this article, the nonlinear sigmoid function, where both the function itself and its derivatives are continuous, is chosen as the activation function. In the forward process, the network calculates the predicted SSH based on the input feature data with the current weights in the network. The second stage is the backpropagation of the mean square error (MSE), which is calculated using the predicted SSH (SSH_{pred}) and the desired SSH (SSH_{DTU}) according to (3), and then the derivative of the loss function for the weights and biases is found. Finally, the Weights and biases between the layers are adjusted sequentially to minimize the MSE between the output and target values

$$MSE = \frac{1}{n} \sum\nolimits_{i=1}^{n} (SSH_{pred} - SSH_{DTU})^2. \quad (3)$$

B. CNN Model

CNN is also a feedforward neural network that uses the backpropagation algorithm and can easily update the data model. CNN is suitable for t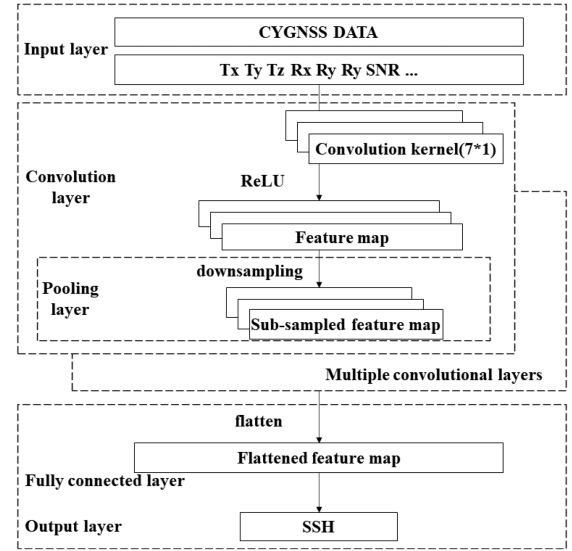raining large amounts of data and can solve complex nonlinear problems. As shown in Fig. 7, the structure of CNN generally consists of an optional set of convolutional layers containing a specific number and size of convolutional kernels, a pooling layer for downsampling compressed data, and a fully connected layer and an output layer [22]. The convolution kernel is a kind of affine transform unit that can calculate feature information from data. The convolution operation of a complex convolution kernel with input data can obtain in-depth data information. The convolutional output is further processed by an activation function with nonlinear capabilities to obtain new feature data. After that, the pooling layer can be chosen to compress the data and eliminate data redundancy by downsampling. Finally, the neural network with a fully connected layer is used to combine all the features learned earlier to transform the data from high to low dimensions and output classification or regression results. In this article, pooling layers are not used in order to avoid the loss of data information as much as possible. Convolutional layers can be multiple, and after that, a fully connected layer is used to combine the previously learned features. This is also the most significant difference from BP neural networks. In terms of the number of layers in the network, CNN is deeper due to the introduction of convolutional layers.

IV. RESULTS AND ANALYSIS

A. SSH Performance of the ML Models With DTU Data

Based on experience, this article searches for the best network structure among BP networks with 1-2 hidden layer structures. Finally, it determines that a structure with 2 hidden layers and 50 nodes per layer is more suitable for the feature dataset of this article.

Fig. 8(a) shows the statistical results and the degree of fit of the BP model for the SSH inversion on each GPS satellite subdataset. BP model fits well, with MAE at about 1 m and
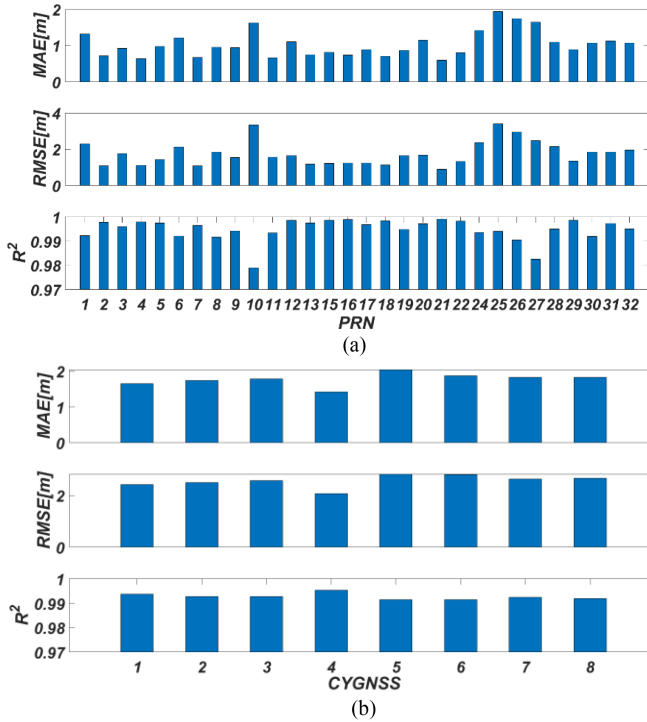
Fig. 8.   Results of BP model on: (a) GPS satellite subdataset; (b) CYGNSS satellite subdataset.

Fig. 9.   Results of CNN model on: (a) GPS satellite sub-dataset; (b) CYGNSS satellite sub-dataset.

RMSE at about 2 m. Among them, satellites 1, 10, 24, 25, 26, and 27 performed relatively poorly. Fig. 8(b) shows the statistical performance of the BP model on each CYGNSS subdataset. The BP models also fit well, with MAE around 1.5 m and RMSE around 2.5 m, and each CYGNSS satellite has similar accuracy. The amount of data is an important cause of differences and similarities in performance, and the more considerable the amount of data, the more likely it is that a better model can be obtained. Normally, the strategy of dividing the data according to the GPS satellite PRN is better than dividing them according to the CYGNSS satellite number.

Empirically, this article utilized similar combinations of hyperparameter permutations for the CYGNSS feature dataset to search for the best hyperparameter combinations for the CNN model. Finally, the convolutional kernel size of 7×1 and the number of 64 convolutional layers are considered the best-performing structure.

Fig. 9(a) shows the statistical results and the degree of fit of the CNN model for the inversion of SSH on each GPS satellite subdataset. CNN model fits well, with MAE below 1 m and RMSE below 2 m for most of the subdatasets. Comparing the amount of data, the model did not perform poorly on the dataset with less data. Even with a small amount of data, CNN can mine more information about the data. Fig. 9(b) shows the statistical performance of the CNN model on each CYGNSS subdataset. The models also fit well, with MAE around 1 m and RMSE around 2 m, and each CYGNSS satellite has similar accuracy. Normally, the strategy of dividing the data according to the
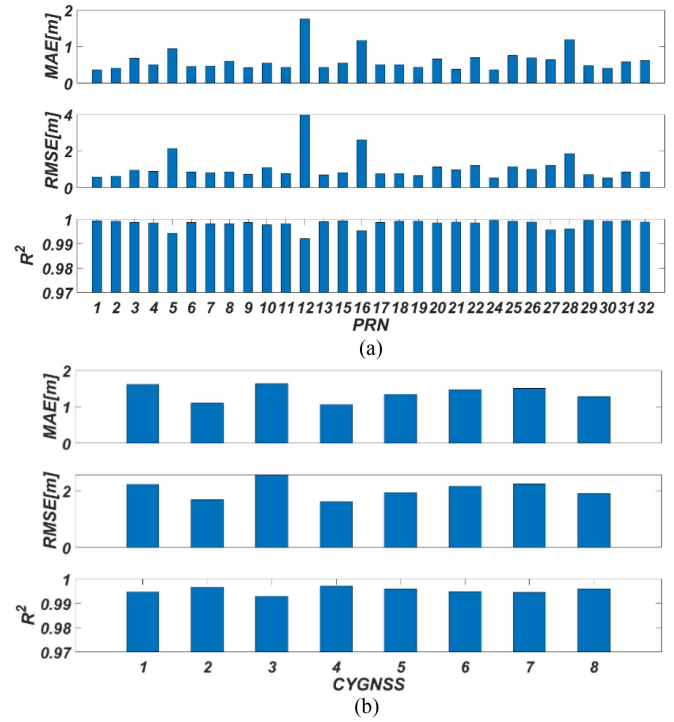
GPS satellite PRN is better than dividing them according to the CYGNSS satellite number.

Table II summarizes the average performance of the two models. According to the division strategy of the GPS satellite PRN, the MAE of the BP model is 1.04 m, and the RMSE is 1.76 m. The MAE of the CNN model is 0.63 m, and the RMSE is 1.10 m. According to the division strategy of CYGNSS satellite number, the MAE of the BP model is 1.77 m, and the RMSE is 2.57 m. The MAE of the CNN model is 1.38 m, and the RMSE is 2.04 m. The strategy of dividing the dataset by GPS satellite PRN for independent analysis is more suitable for the ML model to perform SSH inversion of CYGNSS data, so in the subsequent analysis, only the strategy of dividing the dataset by GPS satellite PRN will be used. The inversion errors of both models for SSH are within the expected range, and the accuracy of CNN is always better than that of the BP model. This not only confirms the effectiveness of SSH inversion of CYGNSS data using ML methods but also shows the advantages of the CNN method of deep learning in this article.

TABLE II
AVERAGE ACCURACY OF INVERSION SSH RESULTS WITH DTU DATA

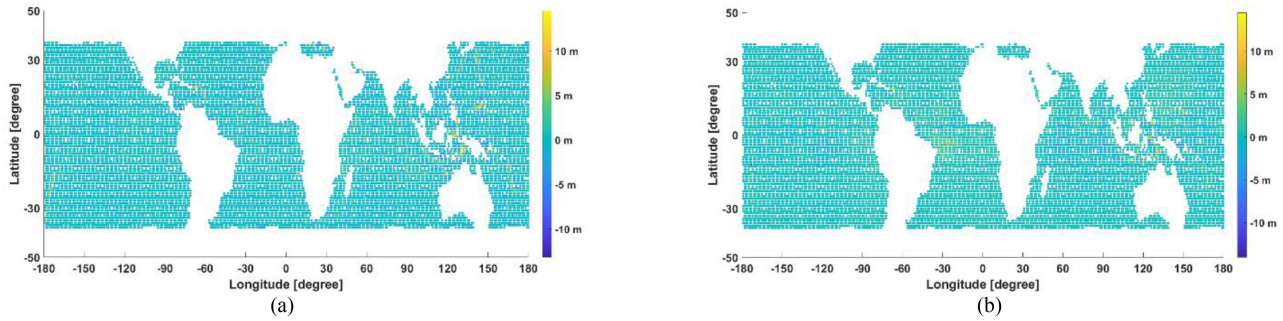| Method	according to GPS satellite PRN		according to CYGNSS satellite number	
	MAE(m)	RMSE(m)	MAE(m)	RMSE(m)
BP	1.04	1.76	1.77	2.57
CNN	0.63	1.10	1.38	2.04

Fig. 10. Compared with the CLS 2015, the average MSSH error of the BP model (a) and the CNN model (b).
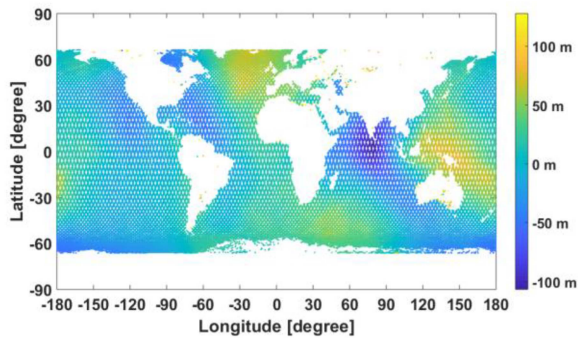
Fig. 11. Jason-3 calculated MSSH results distribution.

TABLE III
AMOUNT OF GENERALIZATION DATA SETS (6 DAYS)

	2020.8.1~2020.8.6 (training set)		2020.8.7 (test set)
	training data	validation data	test data
PRN2	183 002	183 002	67636
PRN4	202 905	202 905	61001

B. Average Grid MSSH Comparison With MSS CLS 2015 and Jason-3 Data

The inversion results of CYGNSS data by the ML model are statistically separated according to the one-degree spatial distribution of the earth's latitude and longitude after removing the influence of ocean tides uniformly using the DTU global ocean tide model. Then the one-degree grid average MSSH value and the difference from the CLS 2015 model are calculated.

Fig. 10 shows the distribution of the inversion error of the BP model and the CNN model, respectively. The maximum absolute value of the error does not exceed 10 m, and the error in most areas is close to 0 m. The MAE of the BP model is 0.61 m, and that of the CNN model is 0.5 m, indicating that the performance of the CNN model is better than the BP model with CLS 2015 data.

In this article, Jason-3 data for the same period as CYGNSS, August 1–7, 2020, totaling about 740 000, were downloaded. After data filtering for outliers, a total of over 730 000 data were retained, and Jason-3 MSSH was calculated. Fig. 11 shows the specifics of the calculated Jason-3 MSSH results from (2) distribution, which are spread across the global seas.

After that, there are two steps. First, according to the DTU global ocean tide model, remove the tide height from the inversion SSH from CYGNSS data using two ML models, to obtain the MSSH. Second, calculate the one-degree grid average CYGNSS MSSH results and the one-degree grid average Jason-3 MSSH results. Fig. 12 shows the distribution of the inversion error of the BP model and the CNN model, respectively. The

maximum absolute value of the error is about 10 m, and the error in most areas is close to 0 m. The MAE of the BP model is 0.84 m, and that of the CNN model is 0.78 m, indicating that the performance of the CNN model is also better than BP model with the Jason-3 data.

As shown in Figs. 10 and 12, there are significant deviations for both ML models in some areas. First, some regions such as near Indonesia, have a lower density of revisit points and less data compared to other areas, which is detrimental to ML. Fig. 13 shows the lower density of revisit points around Indonesia (red box). Second, many poorly performing areas are close to the coast, especially in Indonesian waters, which makes the data subject to more complex external environmental factors, such as tides [2]. Third, although most of the bad data are filtered out, there are still some poor-quality DDMs that are difficult to find by quality flags. Fig. 14 shows some DDMs in these areas with bad delay waveforms, probably influenced by wind waves. In addition, ML is a data-driven algorithm, and the amount of anomalies is relatively small and thus cannot be handled by ML algorithm. Therefore, the poor performance of ML methods on outliers is really unavoidable.

C. Generalization Ability of the ML Models

In order to evaluate the generalization ability of the ML models, two training sets are used to predict a new day's SSH (August 7, 2020). One is from August 1–6, 2020 for a total of 6 days and the other is from July 25–August 6, 2020, for a total of 13 days. For 6 days set (August 1–6, 2020), the training set is further randomly divided into two subsets, training data, and validation data. The PRN2 and PRN4 satellites, which have more data volume and more uniform time distribution, are taken
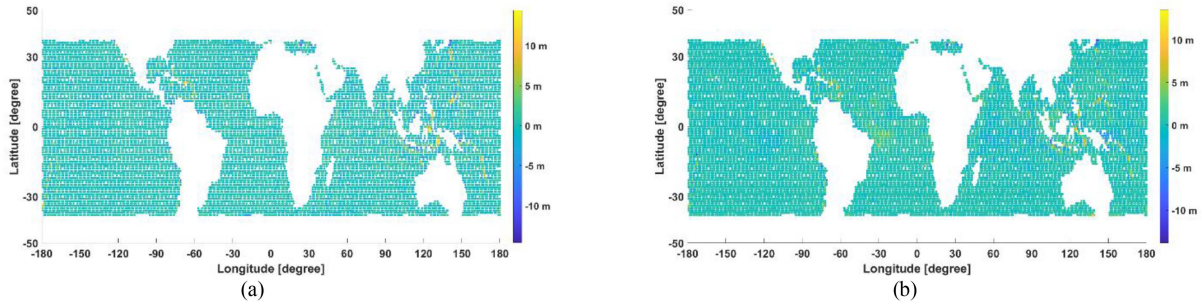
Fig. 12.   Compared with the Jason-3, the average MSSH errors of the BP model (a) and the CNN model (b).
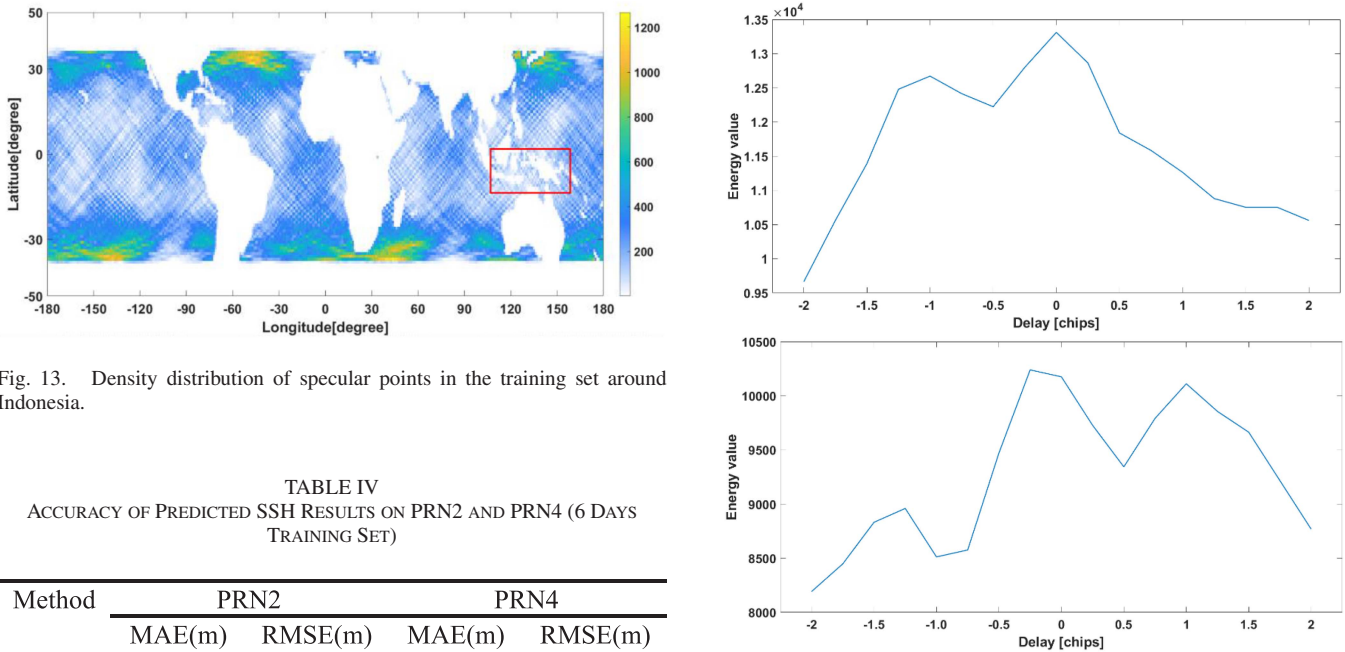

Fig. 13.   Density distribution of specular points in the training set around Indonesia.

TABLE IV
ACCURACY OF PREDICTED SSH RESULTS ON PRN2 AND PRN4 (6 DAYS TRAINING SET)

Method	PRN2		PRN4	
	MAE(m)	RMSE(m)	MAE(m)	RMSE(m)
BP	11.59	15.05	5.90	8.06
CNN	1.37	2.41	0.97	1.63

Fig. 14.   Some of the poor-performing DDMs with bad delay waveforms.

as examples. Table III shows the generalization data set number of 6 days.

For the 6 days training set, Figs. 15 and 16 show the CYGNSS satellite flight track and corresponding forecast SSH error of BP and CNN model on PRN2 and PRN4, where the error is the difference between the predicted result and the DTU SSH model. Fig. 17 shows the error of the BP and CNN model on PRN2 and PRN4. These three figures contain all the tracks predicted for the day of August 7, 2020. The sequence of the samples is based on the sequence of the tracks. And the sequence of the tracks is ordered by CYGNSS satellite number. The prediction results' MAE of the BP model is 11.59 m and 5.90 m for PRN2 and PRN4, and the MAE of the CNN model is 1.37 m and 0.97 m for PRN2 and PRN4, respectively. Table IV shows the prediction accuracy of the two models built with 6 days training set on PRN2 and PRN4.

The accuracy of the BP model is relatively poor and unstable. In contrast, the CNN model has no steep drop in accuracy and

performs relatively more stable in the generalization study. This also illustrates the more robust generalization performance of the CNN model on CYGNSS data, which further highlights the advantage of the deep learning capability of the CNN approach. Compared with the traditional methods, the BP model is less generalizable, while the CNN model has a higher prediction potential for future data. This may be caused by the difference in the degree of data information mined by the models.

To explore the performance of the model built with more data, a new training set from July 25–August 6, 2020, for a total of 13 days was selected. Table V shows the amount of the new generalization data set. For the 13 days training set, the prediction results' MAE of the BP model is 11.72 m and 9.80 m for PRN2 and PRN4, and the MAE of the CNN model is 1.43 m and 0.98 m for PRN2 and PRN4, respectively. Table VI shows the prediction accuracy of the two models built with 13 days training set on PRN2 and 4.
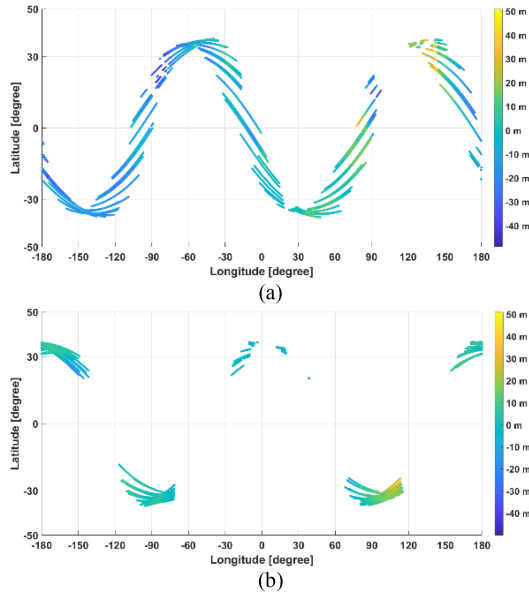
Fig. 15. CYGNSS satellite flight track and corresponding forecast SSH error of the BP model (August 7, 2020): (a) PRN2; (b) PRN4.
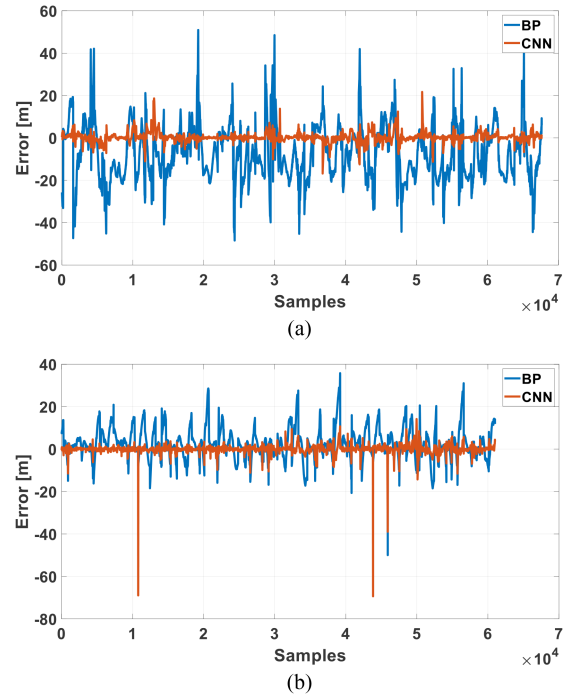

Fig. 16. CYGNSS satellite flight track and corresponding forecast SSH error of the CNN model (August 7, 2020): (a) PRN2; (b) PRN4.

Fig. 17. Forecast SSH errors relative to DTU data of the BP and CNN model: (a) PRN2; (b) PRN4.
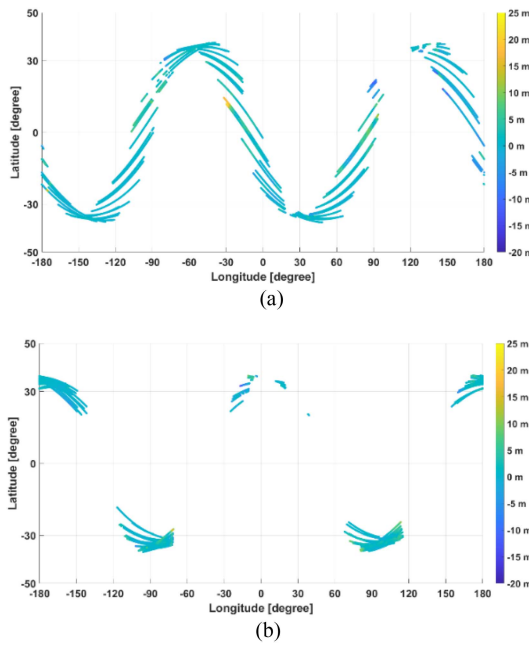

Fig. 18. Data distribution of the PRN2 training set: (a) 6 days; (b) 13 days.

TABLE V
AMOUNT OF NEW GENERALIZATION DATA SETS (13 DAYS)

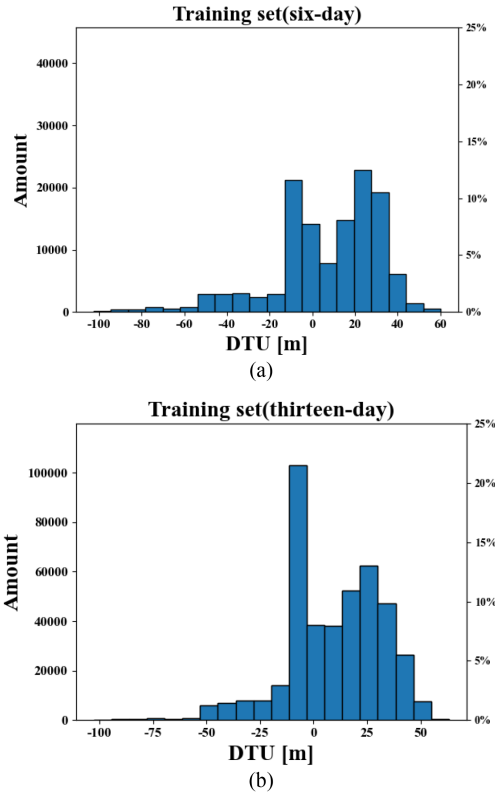|	2020.7.25~2020.8.6 (training set)		2020.8.7 (test set)
	training data	validation data	test data
PRN2	388 190	388 190	67636
PRN4	479 531	479 531	61001

Fig. 19.　Data distribution of the PRN4 training set: (a) 6 days; (b) 13 days.

TABLE VI
ACCURACY OF PREDICTED SSH RESULTS ON PRN2 AND PRN4 (13 DAYS TRAINING SET)

Method	PRN2		PRN4	
	MAE(m)	RMSE(m)	MAE(m)	RMSE(m)
BP	11.72	14.24	9.80	13.16
CNN	1.43	2.48	0.98	1.52

As shown in Tables IV and VI, increasing the data volume does not improve the inversion accuracy, it may be mainly for the following reasons: First, the current hyperparameters are based on 6 days training set, so the hyperparameters need to be further optimized and adjusted for 13 days training set. Second, as shown in Figs. 18 and 19, the amount and proportion differences between each SSH interval of the 13 days training set are significantly larger than that of the 6 days training set.

Compared with TDS-1 data, CYGNSS data has the advantage of having a larger number of valid samples. One problem of ML methods is the relatively poor generalization ability. By using appropriate and valid data as well as adding DDM-related features, CYGNSS data has a better generalization performance compared to TDS-1 data in SSH inversion [21].

V. CONCLUSION

In the field of ocean altimetry, ML is less applied due to the many factors affecting SSH. This article proposed for the first time ML models for SSH inversion using CYGNSS data,

and demonstrated the availability and generalization ability of the ML approach to CYGNSS DDM inversion of SSH. It is a preliminary attempt of ML in monitoring the availability of sea level dynamic changes.

CYGNSS data were selected as the input and some ocean-related data products were selected to validate the output SSH. The article aims to mine the mapping relationship between SSH and CYGNSS data from the data itself, two ML methods, BP and CNN were selected and compared. Based on various ocean data products, SSH and MSSH validation models were developed for evaluation.

First, to investigate the fitting ability of the ML models, CYGNSS data from 7 days data (August 1–7, 2020) were selected for the experimental analysis, and as much valid data information related to SSH as possible were selected. The 7 days data were randomly divided into a training set with 20% data to train the ML SSH inversion models and a testing set with 80% data to evaluate the ML models' performance. The results of multiple data partitioning strategies and evaluation strategies are also discussed. The strategy of dividing the data according to the GPS satellite PRN numbers is better than dividing them according to the CYGNSS satellite numbers: both the BP and CNN models exhibit good inversion performance, the MAE of 1.04 m for the BP model and 0.63 m for the CNN model are achieved. For average grid MSSH validation models, the ML models are still performing well. Compared with the CLS 2015 data, the MAE of the BP model is 0.61 m, and that of the CNN model is 0.5 m. Compared with the Jason-3 data, the MAE of the BP model is 0.84 m, and that of the CNN model is 0.78 m.

Second, to investigate the generalization ability of the ML models, two training sets are used for building ML SSH inversion models, and the SSH of a new day was predicted by the built models. One training set consists of 6 days data (August 1–6, 2020), and the other consists of 13 days data (July 25–August 6, 2020). On the 6 days training set, the MAE of 11.59 m and 5.90 m for the BP model, 1.37 m and 0.97 m for the CNN model are obtained on PRN2 and PRN4, respectively. On the 13 days training set, the MAE of 11.72 m and 9.81 m for the BP model, 1.43 m and 0.98 m for the CNN model are obtained on PRN2 and PRN4, respectively. Though the performance of the BP and CNN models is weakened in the generalization ability, CNN methods in the field of deep learning still have some advantages and potential in terms of accuracy.

Though the ML SSH inversion models built in this article, especially CNN models, meet the expected accuracy, there are still related elements that need to be studied. Compared with the traditional SSH inversion methods, the ML methods have the advantages of not having to consider building error models and being able to adequately construct mapping relationships between original physical parameters and SSH. However, getting feature parameters is manual and somehow subjective. In the future, by adding external environmental features, and using more advanced ML methods, the ML models may have better performance in the study of mesoscale phenomena of the sea surface (such as eddies). Although space-borne GNSS-R observations have higher temporal resolution and wider spatial distribution, the topic of how to use the data collected by TDS-1,

CYGNSS, and other satellites to predict unknown future SSH on a large spatial and temporal scale is still a challenge.

Acknowledgment

References

[1] M. Martin-Neira, "A passive reflectometry and interferometry system (PARIS): Application to ocean altimetry," *ESA J.*, vol. 17, no. 4, pp. 331–335, 1993.

[2] Z. Yun, L. Binbin, T. Luman, G. Qiming, H. Yanling, and H. Zhonghua, "Phase altimetry using reflected signals from beidou GEO satellites," *IEEE Geosci. Remote Sens. Lett.*, vol. 13, no. 10, pp. 1410–1414, Oct. 2016.

[3] Y. Zhang, L. Tian, W. Meng, Q. Gu, Y. Han, and Z. Hong, "Feasibility of code-level altimetry using coastal beidou reflection (BeiDou-R) setups," *IEEE J. Sel. Topics Appl. Earth Observ. Remote Sens.*, vol. 8, no. 8, pp. 4130–4140, Aug. 2015.

[4] A. A. Arroyo et al., "Dual-polarization GNSS-R interference pattern technique for soil moisture mapping," *IEEE J. Sel. Topics Appl. Earth Observ. Remote Sens.*, vol. 7, no. 5, pp. 1533–1544, May 2014, doi: 10.1109/JS-TARS.2014.2320792.

[5] X. Peng, X. Chen, H. Xiao, W. Wan, T. Yang, and Z. Yang, "Estimating soil moisture content using GNSS-R technique based on statistics," in *Proc. IEEE Int. Geosci. Remote Sens. Symp.*, 2015, pp. 2004–2007, doi: 10.1109/IGARSS.2015.7326191.

[6] Y. Zhang et al., "Detection of Bohai Bay sea ice using GPS-reflected signals," *IEEE J. Sel. Topics Appl. Earth Observ. Remote Sens.*, vol. 8, no. 1, pp. 39–46, Jan. 2015, doi: 10.1109/JSTARS.2014.2357894.

[7] Y. Zhang et al., "Sea ice thickness detection using coastal BeiDou reflection setup in Bohai Bay," *IEEE Geosci. Remote Sens. Lett.*, vol. 18, no. 3, pp. 381–385, Mar. 2021, doi: 10.1109/LGRS.2020.2980106.

[8] Y. Zhang et al., "Antarctic sea ice detection using a shipborne GPS reflectometry setup," *Meas. Control*, vol. 54, no. 5/6, pp. 618–626, May 2021.

[9] X. Zhou et al., "Sea surface wind speed measurement using GNSS reflection signal," *J. Electron. Inf. Technol.*, vol. 35, no. 7, pp. 1575–1580, Jul. 2013.

[10] W. Li et al., "Initial results of typhoon wind speed observation using coastal GNSS-R of beidou GEO satellite," *IEEE J. Sel. Topics Appl. Earth Observ. Remote Sens.*, vol. 9, no. 10, pp. 4720–4729, Oct. 2016, doi: 10.1109/JSTARS.2016.2523126.

[11] C. S. Ruf et al., "New ocean winds satellite mission to probe hurricanes and tropical convection," *Bull. Amer. Meteorol. Soc.*, vol. 97, no. 3, pp. 385–395, 2016.

[12] M. Unwin, P. Jales, J. Tye, C. Gommenginger, G. Foti, and J. Rosello, "Spaceborne GNSS-reflectometry on techdemosat-1: Early mission operations and exploitation," *IEEE J. Sel. Topics Appl. Earth Observ. Remote Sens.*, vol. 9, no. 10, pp. 4525–4539, Oct. 2016.

[13] M. P. Clarizia et al., "First spaceborne observation of sea surface height using GPS-reflectometry," *Geophysical Res. Lett.*, vol. 43, no. 2, pp. 767–774, 2016.

[14] H. Qiu and S. Jin, "Global mean sea surface height estimated from spaceborne cyclone-GNSS reflectometry," *Remote Sens.*, vol. 12, no. 3, p. 356, 2020.

[15] Y. Zhang et al., "Research on sea surface height inversion of GPS reflected signal based on TechDemoSat-1," *J. Beijing Univ. Aeronaut. Astronaut.*, vol. 47, no. 10, pp. 1941–1948, 2021.

[16] J. Reynolds, M. P. Clarizia, and E. Santi, "Wind speed estimation from CYGNSS using artificial neural networks," *IEEE J. Sel. Topics Appl. Earth Observ. Remote Sens.*, vol. 13, pp. 708–716, Feb. 2020, doi: 10.1109/JS-TARS.2020.2968156.

[17] Y. Zhang et al., "High wind speed inversion model of CYGNSS sea surface data based on machine learning," *Remote Sens.*, vol. 13, no. 16, Aug. 2021, Art. no. 3324.

[18] Y. Zhang et al., "Wind direction retrieval using support vector machine from CYGNSS sea surface data," *Remote Sens.*, vol. 13, no. 21, Nov. 2021, Art. no. 4451.

[19] V. Senyurek et al., "Machine learning-based CYGNSS soil moisture estimates over ISMN sites in CONUS," *Remote Sens.*, vol. 12, no. 7, 2020, Art. no. 1168.

[20] Q. Wang et al., "A new GNSS-R altimetry algorithm based on machine learning fusion model and feature optimization to improve the precision of sea surface height retrieval," *Front. Earth Sci.*, vol. 9, 2021, Art. no. 758.

[21] Y. Zhang et al., "Machine learning methods for spaceborne GNSS-R sea surface height measurement from TDS-1," *IEEE J. Sel. Topics Appl. Earth Observ. Remote Sens.*, vol. 15, pp. 1079–1088, Dec. 2022, doi: 10.1109/JS-TARS.2021.3139376.

[22] H. Tayara, K. G. Soo, and K. T. Chong, "Vehicle detection and counting in high-resolution aerial images using convolutional regression neural network," *IEEE Access*, vol. 6, pp. 2220–2230, 2018.

Yun Zhang received the Ph.D. degree in applied marine environmental studies from Tokyo University of Maritime Science and Technology, Tokyo, Japan, in 2008.

From 2011, he is a Professor with the College of Information and Technology, Shanghai Ocean University, Shanghai, China. His research interests include the study of navigation system reflection signal technique and its maritime application.

Qi Lu received the B.S. degree in computer science and technology in 2020 from Shanghai Ocean University, Shanghai, China, where he is currently working toward the M.E. degree in computer technology.

He is in research on remote sensing with Global Navigation Satellite Systems-Reflectometry of sea surface height.

Qin Jin received the master's degree in the major of electronic communication engineer from Beihang University, Beijing, China, in 2013.

She is a Junior Engineer in 2013, and become an Intermediate Engineer in 2015, and then a Senior Engineer in 2019, with the Shanghai spaceflight institute of TT&CT. Her research interests include passive microwave remote sensor and communication payload design and manufacture.

Wanting Meng received the B.S. degree in spatial information and digital technology and the M.S. degree in software engineering from Shang Ocean University, Shanghai, China, in 2013 and 2016, respectively.

She is currently with Shanghai Spaceflight Institute of TT&C and Telecommunication, Shanghai, China, where she is currently a Research Associate in the field of microwave radiometer calibration techniques and GNSS-R remote sensing.
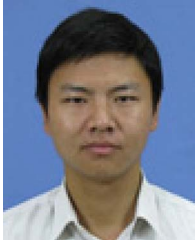
Shuhu Yang received the Ph.D. degree in physics of physics from the School of Physics, Nanjing University, Nanjing, China, in 2012.

Since Sep. 2012, he has been the Lecturer with the College of Information Technology, Shanghai Ocean University. His research interests include evolution of the Antarctic ice sheet, hyperspectral remote sensing, and the use of navigational satellite reflections.

Zhonghua Hong received the Ph.D. degree in geographical information science from Tongji University, Shanghai, China, in 2014.

He has been an Associate Professor with the College of Information Technology, Shanghai Ocean University, Shanghai, China, since 2019. His research interests include three-dimensional damage detection, coastal mapping, photogrammetry, GNSS-R, and deep learning.

Shen Huang received the B.S. degree in computer science and technology from Nantong University, Nantong, China, in 2018, and the M.E. degree in computer technology from Shanghai Ocean University, Shanghai, China, in 2022.

His research interest includes remote sensing with GNSS-R of sea surface height.

Zhansheng Chen received the B.E. and M.E. degrees in welding technology and engineering from Shanghai Jiaotong University, Shanghai, China, in 1992 and 1995, respectively.

Since 2020, he has been the Director with Shanghai Institute of Satellite Engineering Developing Remote Sensing Satellite Technology, Shanghai, China. His current research interests include satellite system design, intelligent cluster, remote sensing technology applications, and satellite data processing.

Yanling Han received the B.E. degree in mechanical design and manufacturing and the M.E. degree in mechanical automation from Sichuan University, Sichuan, China, and the Ph.D. degree in engineering and control theory from Shanghai University, Shanghai, China, in 1996, 1999, and 2005, respectively.

She is a Professor and currently with the Shanghai Ocean University, Shanghai, China. Her research interests include the study of ocean remote sensing, flexible system modeling, and deep learning.

Weiliang Liu received the master's degree in aerospace propulsion theory and engineering from Beihang University, Beijing, China, in 2005.

He is the CEO with the Shanghai SastSpace Technology Co., Ltd., China. He has been engaged in the research and development of satellites for a long time and committed to the popularization and promotion of satellite applications. He completed the development and launch of GNSS-R satellite and promoted its in orbit application and successively won lots of national science and technology progress award.